Assessment of different {RANS} turbulence models in mini-channels for the cooling of {MW}-class gyrotron resonators

Original
Assessment of different {RANS} turbulence models in mini-channels for the cooling of {MW}-class gyrotron resonators / Difonzo, R., Gajetti, E., Savoldi, L., Fathi, N.. - In: INTERNATIONAL JOURNAL OF HEAT AND MASS TRANSFER. - ISSN 0017-9310. - ELETTRONICO. - 193:(2022), p. 122922. [10.1016/j.ijheatmasstransfer.2022.122922]

Publisher:
PERGAMON-ELSEVIER SCIENCE LTD

Published
DOI:10.1016/j.ijheatmasstransfer.2022.122922

Assessment of different RANS turbulence models in mini-channels for the cooling of MW-class gyrotron resonators

R. Difonzo[1], E. Gajetti[1], L. Savoldi[1][1], N. Fathi[2, 3]
[1]*MATHEP Research Group, Dipartimento Energia "Galileo Ferraris", Politecnico di Torino, Torino, Italy*
[2] *Texas A&M University, TX, USA*
[3]*University of New Mexico, NM, USA*

ABSTRACT

The adoption of high-speed water flow in mini-channels is a viable option for the cooling system of the resonant cavity in gyrotrons, which are a candidate technology for the external plasma heating in nuclear fusion reactors. The evaluation of the performance of such mini-channel cooling system is a combined fluid dynamics and heat transfer phenomenon which seeks more attention to a highly accurate computational analysis. In this study, a computational-based comparative platform is proposed to evaluate the performance and fidelity of the applied turbulence models which are utilized to study the mini-channel cavity cooling systems in gyrotrons. A full-size mock-up of the gyrotron resonator equipped with mini-channels has been realized and tested in 2019 by THALES to check its total pressure drop applying a wide range of water flow rates, including that available for the gyrotron operation. In parallel, a numerical model of the mock-up has been developed using the commercial software STAR-CCM+, and simulations have been performed using different RANS turbulence closures, and namely: SST $\kappa-\omega$, realizable $\kappa-\varepsilon$ and Lag EB $\kappa-\varepsilon$. The detailed comparison of the computed hydraulic characteristics (i.e., a range of pressure drop measurements at different flow rates) to the set of measured values has been addressed using a multivariate metric to assess the performance of different turbulence models in pure hydraulic simulations. This comparative platform reveals a significant clarified difference in fidelity among the RANS models. Based on the performed comparative studies against the entire set of available experimental data, the Lag EB $\kappa-\varepsilon$ closure provides the best performance among the other turbulence models and can be applied for the future studies of the mini-channel cavity cooling systems of the gyrotron resonators.

Keywords: gyrotron resonator, mini-channels, CFD, RANS models, multivariate metric, model validation

---

[1] Corresponding author: laura.savoldi@polito.it.

Nomenclature

a	coefficient
C	coefficient
d	pipe diameter
df	degrees of freedom
D	experimental data
e	roughness
er	error
E	multivariate metric
f	friction factor
F	generic function
GCI	grid convergence index
h	average cell size
L	pipe length
$\dot{m}$	mass flow rate
p	pressure
P	production term
r	ratio
$\boldsymbol{s}$	strain rate tensor
S	simulation result
T	temperature
u	uncertainty
$\bar{\mathbf{v}}$	velocity
$\boldsymbol{V}$	covariance matrix
$\boldsymbol{w}$	vorticity tensor
x	generic input variable
X	sensitivity coefficients vector
y+	dimensionless wall distance
α	elliptic blending factor
β	coefficient
γ	coefficient
Γ	generic transported quantity
Δp	pressure drop
ε	turbulent dissipation rate
$\mathcal{E}$	comparison errors vector
θ	computed order of convergence
k	kinetic turbulent energy
Λ	additional contribution to transport eq.
μ	dynamic viscosity
ν	kinematic viscosity
ρ	density
σ	model coefficient
τ	turbulent time scale
φ	reduced normal stress
ϕ	generic variable crossing a boundary
χ	chi distribution
ω	specific dissipation rate
Ω	source term
ℓ	turbulent scale
$\mathcal{L}$	least squares function

Subscripts

a	absolute
D	measured data
i	referring to i-th mesh
j	referring to j-th flow rate
mv	multivariate metric
num	numerical
ref	reference
t	turbulent
val	value
Γ	generic transported quantity
ε	turbulent dissipation rate
k	kinetic turbulent energy
μ	dynamic viscosity
φ	reduced normal stress
ω	specific dissipation rate
21	between the first and the second one

Superscript

θ	computed order of convergence
21	between the first and the second one

Acronyms

CAD	computer-aided design
EB	elliptical blending
MC	mini-channels
RANS	Reynolds-Averaged Navier-Stokes
Re	Reynolds number
SST	Shear-Stress Transport

1. Introduction

Gyrotrons are high-power high frequency ($\gtrsim$ 100 GHz) oscillators that are used for the plasma heating in nuclear fusion Tokamaks [1]. As the frequency of the microwave beam injected in the plasma equals the electron rotation frequency in the magnetic field the plasma heating process occurs. Devices operating in the continuous wave (CW) mode with the pulse duration of several hundred seconds for the typical output powers range from 1 MW up to 2MW at 170 GHz are currently foreseen for ITER [2]–[6] and DEMO [7] while a 140 GHz 1.5 MW gyrotron is under design for the W7-X upgrade [8]. Dual-frequency gyrotrons such as those installed at the EPFL in the Tokamak Configuration Variable [9] are also employed in Tokamaks to provide not only plasma heating (Electron Cyclotron Heating) but also current drive (Electron Cyclotron Current Drive) [1] to the plasma.

One of the main components of the gyrotron is the resonant cavity or resonator which is a hollow cylinder (red circle zone in Figure 1) where the interaction between the electron beam and the electromagnetic wave excited inside the cavity takes place. In the cavity, a portion of the kinetic energy of the electron beam emitted by the electron gun is converted into a microwave radiation beam. During the operation, a high heat load with a peak power flux in the order of 20-25 MW/m^2 is deposited on the inner wall of the cavity [1]. The thermal deformation, that arises from the temperature increase due to the heating, could cause a frequency shift, leading in turn to the loss of the microwave beam. In order to contain the effect of the wall heating and, consequently, the impact of the deformation, an efficient cooling system is necessary.

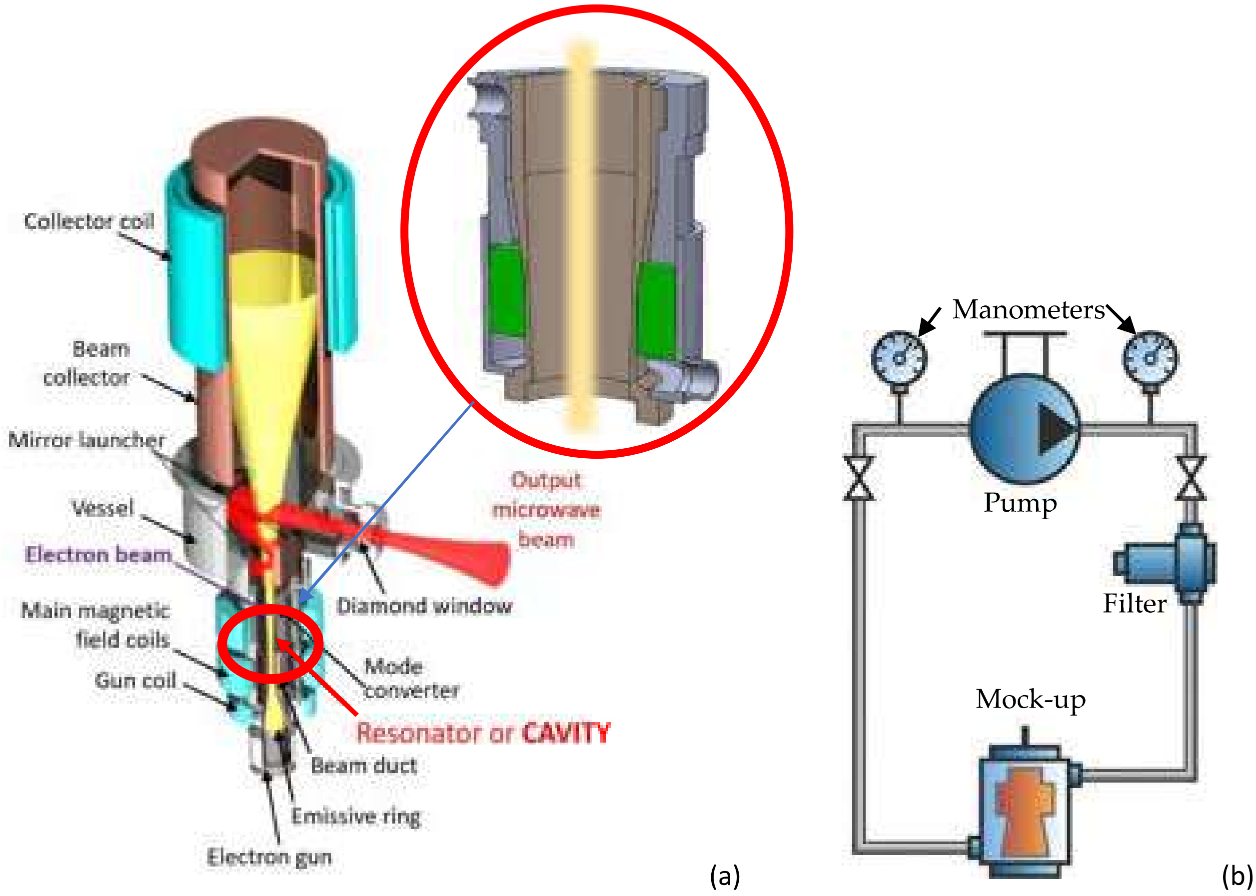

Figure 1: (a) Sketch of a Gyrotron. Modified from [10]. *(b) Sketch of the circuit for the hydraulic tests of the resonator mock-up.*

Active cooling is typically provided on the annular region around the cavity (the green region in the inset in Figure 1a) with subcooled pressurized water. The heat transfer can be enhanced by increasing the wetted surface using, e.g., the metal porous matrix made by brazed Raschig Rings [11], or by increasing the fluid velocity. In fact one of the cooling solutions under consideration for the European gyrotrons for W7-X or DEMO refers to the longitudinal mini-channels (MCs) [12]. In this case a turbulent water flow (Reynolds number ~ 10^4) is utilized to increase the heat transfer coefficient at the cost of an increase in pressure drop. In order to experimentally validate the MC cooling concept and check if the pressure drop across the cavity is acceptable i.e., below 0.5 MPa, which is the maximum allowable pressure drop in the cooling loop where the gyrotron cavity is typically inserted, a mock-up with the cavity equipped with mini-channels has been manufactured by Thales, the leading manufacturer of gyrotrons in Europe. The mock-up, shown in Figure 2, has been tested at the Thales premises in summer 2019 to measure and evaluate its hydraulic characteristics [13].

For cooling applications, where the high speed of the fluid is utilized to enhance and ameliorate the heat transfer, hydro-dynamic phenomena play a key role and a reliable modelling and simulation of the fluid-dynamics is required to accurately predict the cooling efficiency, especially when turbulence is experienced in the system. Since a wide range of turbulence models is available, a careful selection of the turbulence closure to be used in the simulations is very important to achieve more reliable results. This becomes even more significant when the numerical models are used not only to interpret the experimental results, but also as design tools. This is exactly the case of the application at hand here, for which several numerical analyses are ongoing [14]–[16], in order to optimize the MC cooling configuration for the gyrotron cavities. The choice of a reliable turbulence model is here the first step toward a robust model in terms of evaluation of the hydraulic behaviour of the cavity, that is in turn the basis for a reliable evaluation of its thermal behaviour. For a component with water turbulent flow in circular mm-size channels, no studies are currently available that compare the performance of different turbulence models to experimental data, and allows a well-educated selection among them.

The aim of the present investigation is therefore to compare the performance of various types of Reynolds-average Navier Stokes (RANS) turbulence models to evaluate the pressure drops along the gyrotron cavity equipped with a MC cooling system. Among the RANS available models in standard CFD commercial software packages such as STAR-CCM+, specific models are selected as the more suitable models and approaches for the analysis of the case at hand, and namely the cavity mock-up previously mentioned. The computational results from the models applied in this work are initially compared to a classical correlation for the pressure drop in smooth pipes, and then validated against the experimental data measured on the MC mock-up tested at Thales. The validation is performed using a multivariate metric which allows accounting for the correlation among different set points, according to the approach proposed by the ASME V&V20 Committee [17]. The comparison of the different models against the correlations and experimental results allows the selection of the most suitable model, in terms of accuracy of the results, for the simulation of the cavity equipped with MC, at least as far as the pure hydraulic problem is concerned.

The paper is organized as follows: first, the methodology is presented, with a particular reference to the choice of the turbulence models and the multivariate metric adopted for the model comparison and assessment. Then, the selected models are first challenged against the classical Colebrook correlation for the friction factor in circular pipes, and then against the measured data on the MC mock-up. For both cases, the computed results are first presented and then the comparative study among the turbulence models is performed using the multivariate metric.

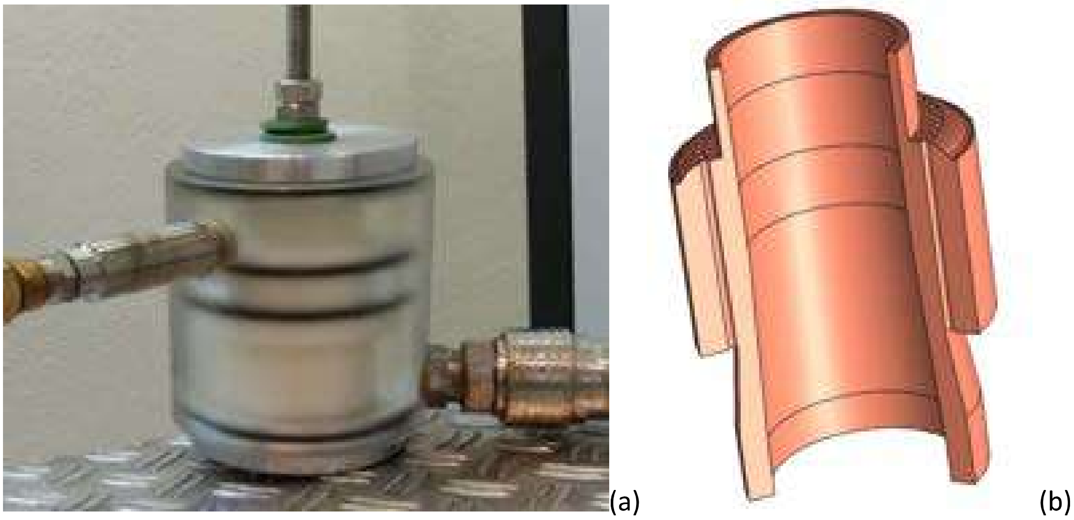

Figure 2: Mock-up of the gyrotron cavity equipped with MCs: (a) picture, (b) CAD model.

2. Methodology

2.1. Selection of RANS turbulence models

The hydraulic simulations of the MC cooling system are performed using the commercial software Star-CCM+ [18]. Among the many RANS models available in the software, the selection of the most suitable RANS turbulence closures for the simulation of the gyrotron cavity equipped with MCs boils down to three models: *Realizable* $k - \varepsilon$, $k - \omega$ *SST and Lag Elliptic Blending* $k - \varepsilon$. The choice has been taken by selecting the most new and performative model out of the two main classes of RANS, leading to select the *Realizable* $k - \varepsilon$ [19], more suitable for application that contains multiple recirculation zones or large streamline curvature than standard version [20], for the $k - \varepsilon$ family, and the $k - \omega$ *SST* [21] out of the $k - \omega$ family, capable to capture not only the near-wall behaviour, but also the core fluid flow. The *Lag Elliptic Blending* $k - \varepsilon$ [22], which is a four equations extension of the $k - \varepsilon$ was selected since it is more recent and with promising prediction for heat transfer problems.

In the general turbulence modelling framework, it is useful to define some invariants related to velocity gradients before proceeding to the description of the characteristic equations: those are the strain rate tensor and the vorticity tensor, defined respectively in Eq. 1 and Eq. 2. In the following their moduli will be referred to as s and w.

$$\boldsymbol{s} = \frac{1}{2}(\nabla\overline{\boldsymbol{v}} + \nabla\overline{\boldsymbol{v}}^{T})$$

Eq. 1

$$\boldsymbol{w} = \frac{1}{2}(\nabla\overline{\boldsymbol{v}} - \nabla\overline{\boldsymbol{v}}^{T})$$

Eq. 2

More specifically, the two transport equations added to the standard RANS equations have the form of Eq. 3, where Γ is the transported quantity, i.e. the turbulent kinetic energy k and the turbulent dissipation rate ε for the $k - \varepsilon$ models, or turbulent specific dissipation rate ω for the $k - \omega$ models. P_{Γ} and Ω_{Γ} are production and source terms, whereas Λ is an additional contribution, specific for each model and transported quantity and σ_{Γ} is a model coefficient [18].

$$\frac{\partial(\rho\Gamma)}{\partial t} + \nabla\cdot(\rho\Gamma\overline{\mathbf{v}}) = \nabla\cdot\left[\left(\mu + \frac{\mu_t}{\sigma_{\Gamma}}\right)\nabla\Gamma\right] + P_{\Gamma} + \Lambda + \Omega_{\Gamma}$$

Eq. 3

In the *Realizable* $k - \varepsilon$ model the turbulent eddy viscosity μ_t is defined as function of the density, of the turbulent kinetic energy and of the turbulent time scale (Table 1), multiplied by a coefficient C_μ and a variable damping function F_μ, which simulates the turbulence decrease near wall. The damping function embeds also the strain rate tensor, the vorticity tensor, k and ε.

Table 1: Turbulent time scale τ for the different models

	τ
$Realizable\ k - \varepsilon$	$\frac{k}{\varepsilon}$
$k - \omega\ \ SST\ Menter$	$\min\left(\frac{1}{\max\left(\frac{\omega}{a^*}, \frac{SF_2}{a_1}\right)}, \frac{C_t}{\sqrt{3}S}\right)$
$Lag\ Elliptic\ Blending$	$\sqrt{\left(\frac{k}{\varepsilon}\right)^2 + \frac{C_t^2 \nu}{\varepsilon}}$

The extra term Λ is depicted in Table 2 for the *Realizable* $k - \varepsilon$ model, as well as for the other models used in this analysis. Therein, ε_0, k_0, ω_0 are ambient turbulent values counteracting turbulent decay while definition of the specific time scale T_0 depends on them.

Table 2: Λ for the different models

	Γ	Λ
$Realizable\ k - \varepsilon$	k	$-\rho(\varepsilon - \varepsilon_0)$
	ε	$\frac{\varepsilon}{k} C_{\varepsilon 1} P_\varepsilon - C_{\varepsilon 2} \frac{k}{k + \sqrt{\nu\varepsilon}}\ \rho \left(k - \frac{\varepsilon_0}{T_0}\right)$
$k - \omega\ \ SST\ Menter$	k	$-\rho\beta^*(\omega k - \omega_0 k_0)$
	ω	$-\rho\beta(\omega^2 - \omega_0^2)$
$Lag\ Elliptic\ Blending$	k	$-\rho(\varepsilon - \varepsilon_0)$
	ε	$\frac{\varepsilon}{k} C_{\varepsilon 3} P_\varepsilon - C_{\varepsilon 4} \rho \left(k - \frac{\varepsilon_0}{T_0}\right)$

The production terms P_ε and P_k depend only on the turbulent production, mean strain rate and turbulent kinetic energy, as neither the buoyancy production neither the compressibility modification are relevant for this problem. Both production terms also contain a curvature correction factor, which could help accounting, in the problem at hand, for the curvature of the fluid moving in the manifold orthogonal to the mini-channels before entering them.

Table 3: Realizable $k-\varepsilon$ Two-layer model coefficients in Star-CCM+

C_t	1
$C_{\varepsilon 1}$	$\max\left(0.43, \frac{\frac{Sk}{\varepsilon}}{5+\frac{Sk}{\varepsilon}}\right)$
$C_{\varepsilon 2}$	1.9
C_μ	0.09
σ_ϵ	1.2
σ_k	1

The *Shear-Stress Transport (SST)* $k-\omega$ *model* [21] is a two-equations eddy-viscosity model which combines the $k-\varepsilon$ and the $k-\omega$ models through a blending function that activates the first one in the free stream and the second one near the wall. It offers good performance typically when the accurate simulation of the viscous sub-layer comes with the need for accurately predicting the flow behavior in regions away from the wall [20]. Eq. 7 is thus defined for both k and ω, for which the production terms P_k and P_ω are composed by turbulent production, non-linear production, specific dissipation production and cross diffusion. Similar to the $k-\varepsilon$ case, the turbulent viscosity depends just on density, turbulent kinetic energy and on $k-\omega$ model-specific turbulent time scale (see Table 1). In the definition of τ, F_2 is a blending function embedding in its formulation, beside ω and k, the distance to the wall, that enables the switching between the two different models, which is peculiar of the $SST\ k-\omega$ model. The model coefficients a^*, a_1 and C_T are defined in Table 4, where F_1 is another blending function behaving similarly to F_2 with the addition of a cross diffusion coefficient between k and ω.

Table 4: $k-\omega$ SST model coefficients in Star-CCM+

a^*	$F_1 + (1 - F_1)$
β	$0.075F_1 + 0.0828(1 - F_1)$
β^*	$0.09[F_1 + (1 - F_1)]$
σ_{k2}	$F_1 + 0.85(1 - F_1)$
σ_ω	$0.5F_1 + 0.856(1 - F_1)$
a_1	0.31
C_t	0.6

In the *Lag Elliptic Blending (EB)* $k-\varepsilon$ *model* [22] a transport equation for the reduced normal stress φ is added to the transport equations for k and ε, which allows the misalignment of the principal axes of the strain-rate and the Reynolds-stress (the "lag" between stress and strain) while still using a linear eddy-viscosity model, depending not only on ρ, k and τ but also on φ and s. It is suitable for incorporating curvature and rotation effects. A small correction to the diffusive term in Eq. 3 leads to the general formulation of transport equations for this specific model as in Eq. 4.

$$\frac{\partial(\rho\Gamma)}{\partial t}+\nabla\cdot(\rho\Gamma\bar{\mathbf{v}})=\nabla\cdot\left[\left(\frac{\mu}{2}+\frac{\mu_t}{\sigma_\Gamma}\right)\nabla\Gamma\right]+P_\Gamma+\Lambda+\Omega_\Gamma \qquad \textit{Eq. 4}$$

In Eq. 4, the only contribution to P_ε and P_k is the turbulent production while P_φ also contain the Reynolds-stress anisotropy tensor. The latter combines the strain rate tensor and a modified vorticity tensor (Eq. 5) to account for anisotropy, that on the contrary is not considered in the pure 2-equations models such as $k-\varepsilon$ and $k-\omega$.

$$\widehat{\boldsymbol{w}}=\mathbf{w}-\frac{1}{s^2}\left(\boldsymbol{s}\frac{D\boldsymbol{s}}{Dt}-\frac{D\boldsymbol{s}}{Dt}\boldsymbol{s}\right) \qquad \textit{Eq. 5}$$

A further diffusion equation for the elliptic blending factor α is included to the set of equations of the *Lag Elliptic Blending* $k-\varepsilon$ model, as reported in Eq. 6, where ℓ is the turbulent scale.

$$\nabla\cdot(\ell^2\,\nabla\alpha)=\alpha-1 \qquad \textit{Eq. 6}$$

The coefficients for the $Lag\ EB\ k-\varepsilon$ model are reported in Table 5.

Table 5: Lag EB model coefficients in Star-CCM+

$C_{\varepsilon3}$	1.44
$C_{\varepsilon4}$	1.9
σ_ε	1.2
σ_k	1
σ_φ	1

2.2. Validation approach: the multivariate metric

In order to compare various types of turbulence models, the quantification of the uncertainties was performed to characterize the numerical results and their errors using the ASME V&V 20-2009 Standard [23]. The first uncertainty is the numerical one due to the mesh size, u_{num}, which is quantified by performing a convergence study. The second uncertainty, u_{input}, represents the effect of the input uncertainties on the computed results. The input uncertainty, u_{input}, is evaluated by mean of a local method which means that the sensitivity coefficient of each parameter affected by uncertainty are evaluated and combined for the computation of u_{input} as explained in [23]. The last uncertainty u_D comes from the experimental data. Once these quantities are computed, it is possible to compare simulations and experimental results, each with its own uncertainties, at each set point. Here all the uncertainties of all the set points are combined in a multivariate metric, namely E_{mv}, allowing to compare the three turbulence models using a single index. According to [17], E_{mv} is obtained from Eq. 7.

$$E_{mv}^2=\mathcal{E}^T\boldsymbol{V}_{val}^{-1}\mathcal{E} \qquad \textit{Eq. 7}$$

Here $\mathcal{E}$ is the vector of the comparison errors of the n set points considered in the analysis, see Eq. 8, and $\boldsymbol{V}_{val}$ is the covariance matrix, which is used to characterize the correlation structure between the estimated uncertainties.

$$\mathcal{E}=\begin{bmatrix}S_1-D_1\\ \vdots\\ S_n-D_n\end{bmatrix} \qquad \textit{Eq. 8}$$

In Eq. 8, S_j and D_j are the simulation result and experimental data of the $j-th$ set point, respectively. The covariance matrix, $\boldsymbol{V}_{val}$, contains the numerical uncertainties, simulation input uncertainties and uncertainties in the measured data. As proposed in [17], when simulation and measurement data are independent, i.e. sharing no error sources, $\boldsymbol{V}_{val}$ is evaluated using Eq. 9, where $\boldsymbol{V}_{num}$, $\boldsymbol{V}_{input}$ and $\boldsymbol{V}_D$ are the covariance matrices due to numerical uncertainties, simulation input uncertainties and uncertainties in the measured data, respectively.

$$\boldsymbol{V}_{val} = \boldsymbol{V}_{num} + \boldsymbol{V}_{input} + \boldsymbol{V}_D \qquad \textit{Eq. 9}$$

The diagonal elements of $\boldsymbol{V}_{num}$, $\boldsymbol{V}_{input}$ and $\boldsymbol{V}_D$ are the square of u_{num}, u_{input} and u_D obtained for each set point, while the off-diagonal elements represent the correlation between the estimated numerical / input/ data uncertainties and are illustrated below.

3. Performance against correlations for pressure drop in smooth tubes

The first assessment of the performance of the three turbulence models has been performed against the value of the friction factor f in the mini-channels, defined by Eq. 10, obtained from the Colebrook correlation for turbulent flow [24] reported in Eq. 11 where an uncertainty of ± 10% is quoted.

$$f = \Delta p \, \frac{d}{L} \frac{2}{\rho \mathrm{v}^2} \qquad \textit{Eq. 10}$$

$$\frac{1}{\sqrt{f}} = -2\, log\left(\frac{e}{3.7D} + \frac{2.51}{Re\sqrt{f}}\right) \qquad \textit{Eq. 11}$$

InEq. 10, Δp is the pressure gradient along the channel, ρ is the fluid density and v is the average velocity across it. In Eq. 11 D is the diameter of the mini-channels, Re the Reynolds number of the flow within the channel and L is the investigated mini-channel length. The parameter ϵ is the wall roughness e is assumed equal zero (smooth pipe).

3.1. Simulation setup and results

The domain of the simulation is a 3D smooth circular tube with the diameter of 1.9 mm, as the mini-channels used for cooling the gyrotron. Note that the 3D domain is strictly speaking not needed here (an axial-symmetric 2D model would be enough), but it was used to have mesh consistency with the simulations performed on the mock-up.

A pipe with the length of 5 mm has been used, with periodic interface between inlet and outlet in order to achieve a fully developed turbulent flow. As stated in [18] and [20], a periodic interface is able to connect two physical separated surfaces, so to map one to the other, by setting all the fluxes leaving the first one equal to the fluxes entering the second one. This is performed by posing equal all the variables (generically referred to as ϕ) upstream of the input surface to the variables downstream of the output surface, and vice versa, resulting in $\phi_1 = \phi_{\mathrm{end}-1}$ and $\phi_{\mathrm{end}} = \phi_2$. In Figure 3 the geometry of a mini-channel is shown, with highlight on the different boundaries and definition of the quantities (namely velocity and turbulent variables) crossing the inlet and outlet surfaces.

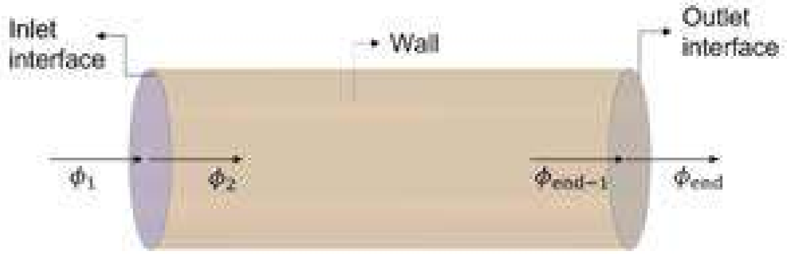

Figure 3: Geometry of the circular channel, with boundaries and upstream/downstream inlet and outlet quantities

Concerning the mesh, polyhedral cells have been used, with a directed mesh (i.e. extruded along the flow direction) to exploit the directionality of the problem, and with a prism layers refinement near the wall in order to achieve values of wall y+ ~1, avoiding thus the use of wall functions in the turbulence models. Figure 4a shows the cross section of the finest mesh implemented for a circular mini-channel, with 12 prism layers at the wall, for a total thickness of 1.5 mm. Water with constant properties at ambient temperature has been adopted as fluid.

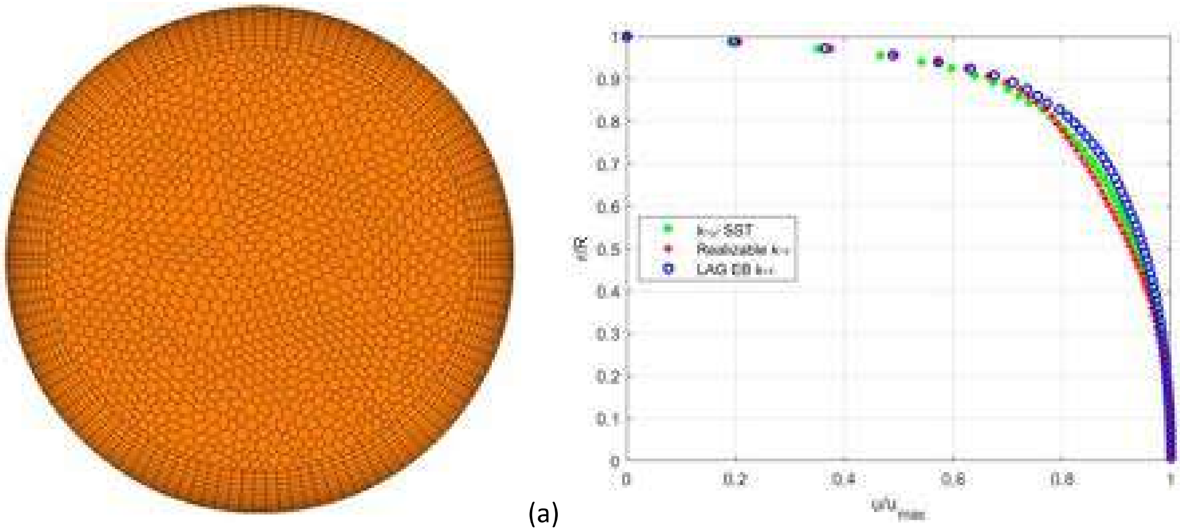

(a) (b)

Figure 4: (a) Finest mesh of the mini-channel. (b) Dimensionless velocity profiles in the pipes vs dimensionless radius, for the lowest flow rate, for the three turbulence models

The study has been carried out by investigating three different values of flow rates (corresponding to 30, 55 and 80 l/min in the totality of the mini-channels mock-up) and simulating five different meshes for each of them with the different turbulence models.

Even with the smallest flow rate, the obtained Re in a single circular mini-channel is higher than the transition Re for inner flow within pipes (equal to ~2200), as it is summarized in Table 6 (volumetric flow rate is referred to the whole cooling device).

The friction factor is extracted from the performed numerical simulations according to Eq. 10. In summary, the computed pressure drop values along the modelled circular mini-channel as well as the computed average velocity of the water flow v are inserted in that expression to estimate friction factors. To check the achievement of a proper turbulent velocity profile within the circular mini-channels, the normalized velocity profiles across the modelled mini-scale tube, computed using the three turbulence models, are represented in Figure 4b for the lowest flow rate of 30 l/min. The expected steep profile at the wall, which flattens at the pipe centre, is computed with all models.

Table 6: Reynolds numbers corresponding to the flow rates

Volumetric flow rate [l/min]	30	55	80
Re	6.95E+03	1.27E+04	1.85E+04

In Figure 5, the friction factors resulting from the Colebrook correlation is reported with the band corresponding to its uncertainty together with the results computed using the different turbulence models for the Reynolds numbers shown in Table 6. The calculated friction factors from numerical simulations are represented together with their numerical error, whose calculation is explained in Section 3.2. Most of the simulation results fall within the accuracy band of the Colebrook correlation, which is consistent with the expectations about the good performance of those models in such a simple geometry. However, from those results we can already remark that the Realizable $k-\varepsilon$ model performs worse compared to the other two turbulence models, at least for the smallest Reynolds number of 6.95E+3 corresponding to the lowest flow rate in Table 6.

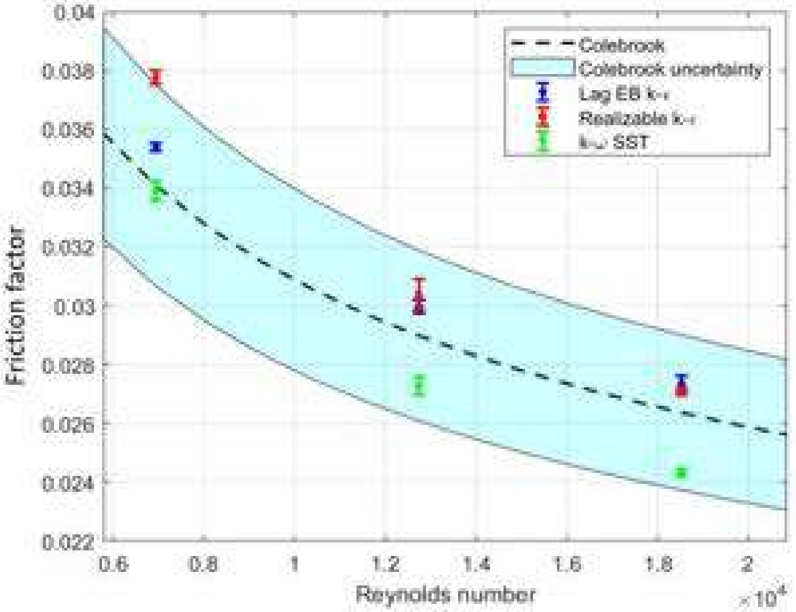

Figure 5: Friction factor vs Reynolds number for different models and compared to the Colebrook correlation.

3.2. Multivariate metric assessment

The evaluation of the three turbulence models against the Colebrook values as the analytical correlation is our interest in this assessment. Therefore, combining all the uncertainties in a single number through multivariate metric was performed. Using multivariate metric allows us to consider the effect of each uncertainty at each flow rate value (set points) as well as their correlations. This provided us with a comparative analysis among the results of the three models which is not local but global in the entire range of the study. As far as the numerical uncertainties are concerned, the simulations performed at the different flow rate values do not share identical error source so the covariance matrix $\boldsymbol{V}_{num}$ is diagonal as in Eq. 12.

$$\boldsymbol{V}_{num} = \begin{bmatrix} u_{num,1}^2 & 0 & 0 \\ 0 & u_{num,2}^2 & 0 \\ 0 & 0 & u_{num,3}^2 \end{bmatrix} \qquad \text{Eq. 12}$$

In order to compute the numerical uncertainty, $u_{num,j}^{2}$ of the simulation results at the $j-th$ flow rate value, a grid independent study has been performed, using five different meshes and the least squares approach to calculate the GCI as suggested in [23]. In Table 7 the parameters of the mesh refinement are listed. The refinement has been carried out simultaneously decreasing the base size and increasing the number of layers in the direction of the flow.

It is assumed that the discretization error generated in this analysis can be expanded with respect to the exact value of the friction factor in a one-term form in Eq. 13:

$$f_i - f_\infty \approx \gamma h_i^{\theta} \qquad \textit{Eq. 13}$$

where f_i is the friction factor computed using the $i-th$ mesh, f_∞ is the extrapolated value, θ is the observed order of convergence and γ is just a coefficient. Note that h_i is the average cell size computed as the cubic root of the ratio between the volume of the domain and the number of cells of the $i-th$ mesh, see Eq. 14.

$$h_i = \sqrt[3]{\frac{Volume}{N_{cells,i}}} \qquad \textit{Eq. 14}$$

The terms f_∞, α, θ can be found by minimizing the least squares function $\mathcal{L}$ defined in *Eq. 15.*

$$\mathcal{L}(f_\infty, \gamma, \theta) = \sqrt{\sum_{i=1}^{5}\left(f_i - \left(f_\infty + \gamma h_i^{\theta}\right)\right)^2} \qquad \textit{Eq. 15}$$

From the computed order of convergence θ, the Grid Convergence Index GCI_j for each flow rate can be computed as in Eq. 16, and finally $u_{num,j}$ is evaluated from Eq. 17.

$$GCI_j = \frac{1.25 \cdot er_{a,j}^{21}}{r_{21,j}^{\theta} - 1} \qquad \textit{Eq. 16}$$

$$u_{num,j} = \frac{GCI_j}{1.15} \qquad \textit{Eq. 17}$$

In Eq. 16, $er_{a,j}^{21}$ is the absolute error between the results using the finest mesh and the second finest mesh. $r_{21,j}^{\theta}$ is the ratio between the cell sizes of the finest mesh and of the second finest mesh and the factor 1.25 is suggested in [23]. Subscript j refers to the $j-th$ flow rate.

Table 7: Mesh parameters for GCI evaluation of the mini-channel pressure drops analysis

Base size [mm]	**# kcells**	**h (average cell size) [mm]**	**r_{i1}**
0.1	76	0.057	1
0.15	31	0.077	1.6
0.17	22	0.087	1.9
0.2	13	0.103	2.4
0.22	8	0.123	3.2

In the model and in the correlation the pipe is perfectly smooth, the diameter of the pipe is perfectly known, as well as the fluid conditions and properties, but the uncertainty associated to the Colebrook correlation is still to be computed. Since the process of deriving the correlation from experimental data could have involved a dataset where the different set points (flow rate values) could have shared common error sources, here two cases are considered:

Case a) assuming that the values of f at the different flow rate values do not share identical error source;

Case b) where the assumption is that the values of f at the different flow rate values share common error source.

The covariance matrix for the Colebrook correlation for Case a) is a diagonal matrix with the square of the value of the uncertainty $u_{D,j}^2$ at the location along the diagonal, being $u_{D,j}$ the uncertainty related to the $j-th$ value of the Colebrook friction factor in Figure 5. For Case b), on the contrary, also the off-diagonal terms must be considered, as shown in Eq. 18.

$$\boldsymbol{V}_D^{(a)} = \begin{bmatrix} u_{D,1}^2 & u_{D,1}u_{D,2} & u_{D,1}u_{D,3} \\ u_{D,1}u_{D,2} & u_{D,2}^2 & u_{D,2}u_{D,3} \\ u_{D,1}u_{D,3} & u_{D,2}u_{D,3} & u_{D,3}^2 \end{bmatrix} \qquad \textit{Eq. 18}$$

Further relevant values to be defined are the expected value $\sqrt{< E_{mv}^2 >}$ and the reference value E_{ref}. The latter allows estimating the mismatch between simulations and the experimental data. Considering the uncertainties of the applied turbulence models can be represented by normal distributions, E_{mv}^2 will be distributed as Chi-squared, $\chi^2(df)$, with the degrees of freedom, *df*, equal to the rank of **V**$_{\mathbf{val}}$ as stated in Eq. 19.

$$< E_{mv}^2 >= \chi^2(df) \ = df \ = 3 \qquad \textit{Eq. 19}$$

For what concerns E_{ref}^2, it is defined in Eq. 20 as the sum of the expected value $< E_{mv}^2 >$ and its uncertainty range, represented by the standard uncertainty of the $\chi^2(df)$ distribution [17]:

$$E_{ref}^2 =< E_{mv}^2 > + \sqrt{\mathrm{var}(E_{mv}^2)} = df + \sqrt{2\ df} \qquad \textit{Eq. 20}$$

The values of the multivariate metric, E_{mv}, resulting from Eq. 7 for the three turbulence models are reported in Figure 6, together with E_{ref} and $\sqrt{< E_{mv}^2 >}$.

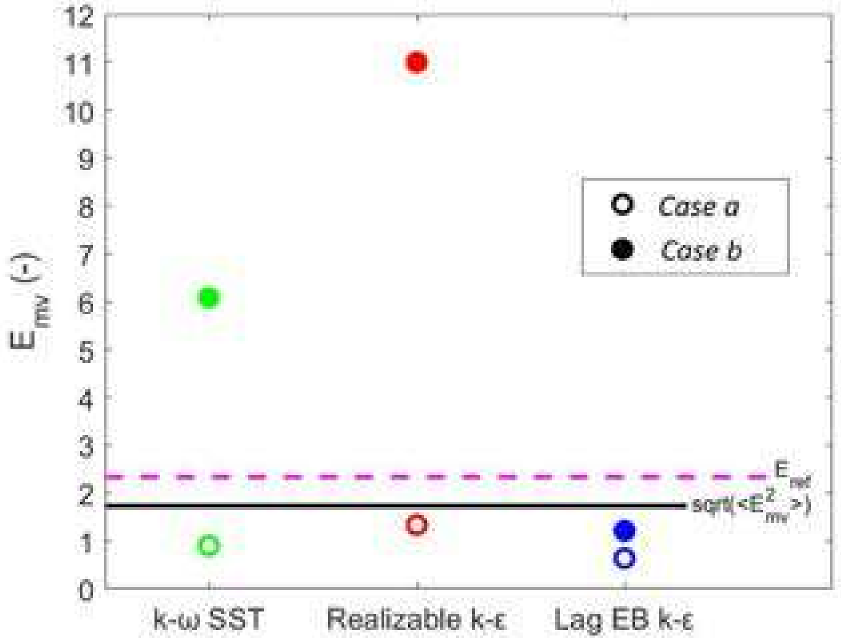

Figure 6: Results for the multivariate analysis on the smooth pipe for the two cases considered

4. Performance against the MC mock-up experimental results

4.1. Experimental results

The test loop for the mock-up hydraulic measurements constituted a pump, connecting pipes, a filter for the water and the mock-up, see Figure 1b. The mock-up includes a nylon prototype of the gyrotron resonator equipped with mini-channels, an external rigid envelope in plastic material, two plugs to close the envelope at top and bottom, two O-rings to keep the resonator in place within the envelope, and two hydraulic connectors to link the mock-up to the test loop, see Figure 2a. The loop instrumentation consisted of two manometers, located upstream and downstream of the pump, and a flow meter, located downstream of the mock-up.

During the experimental measurements, the water flow rate was varied from 30 to 80 l/min (to give turbulent flow in the MCs) and the pressure drop of the loop piping, filter, and the mock-up all together ($\Delta p_{mock-up+loop}$) was measured at each flow rate as the difference of the pressure read-outs measured by the two manometers. After that, in order to calibrate the loop, the mock-up was removed, and the pressure drop of the short-circuited loop only ($\Delta \boldsymbol{p}_{\boldsymbol{loop}}$) was measured again as the difference between the two manometer read-outs. In order to obtain the hydraulic characteristic of the mock-up (Figure 7), for any value of the flow rate the loop pressure drop was subtracted from overall pressure drop following Eq. 21.

$$\Delta \boldsymbol{p}_{\boldsymbol{mock-up}} = \Delta \boldsymbol{p}_{\boldsymbol{mock-up+loop}} - \Delta \boldsymbol{p}_{\boldsymbol{loop}} \qquad \text{Eq. 21}$$

The uncertainty of the experimental data has been evaluated by combining the uncertainties of all the measured variables contributing to the mock-up pressure drop study in the data reduction equation Eq. 7. $\Delta \boldsymbol{p}_{\boldsymbol{mock-up}}$ is obtained by calculating the difference of two pressure drops measured by the manometers of the loop where the pressure read-out on each manometer has an accuracy of ±0.1 bar. Both $\Delta \boldsymbol{p}_{\boldsymbol{mock-up+loop}}$ and $\Delta \boldsymbol{p}_{\boldsymbol{loop}}$ have then a similar uncertainty of ±0.2 bar, but the two uncertainties are not independent. The obtained uncertainty on $\Delta \boldsymbol{p}_{\boldsymbol{mock-up}}$ reported in Figure 7 is also taken thus as ±0.2 bar.

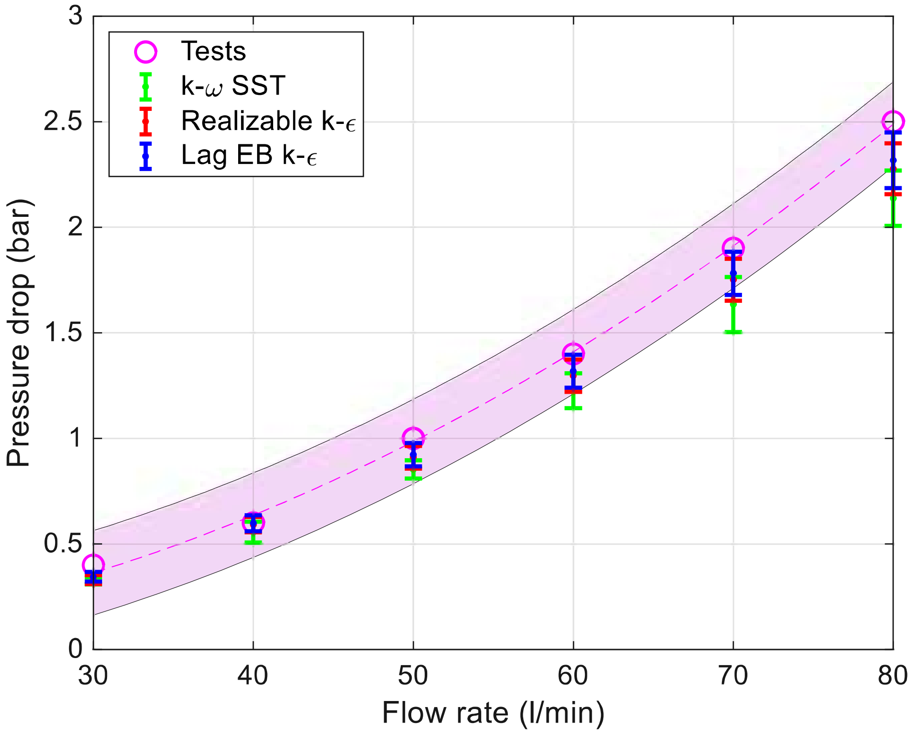

Figure 7: Measured hydraulic characteristic of the mock-up (solid line), Compared to the computed results obtained using the different turbulence models. The uncertainties are reported for both the measurement data and the computed points.

4.2. Simulation setup and computed results

Due to the symmetry of the geometry, only half domain of the mock-up was simulated (see Figure 8a). Constant properties for the fluid (water) at room temperature have been considered since in the test conditions the fluid temperature remains almost constant. A mass flow rate boundary condition was imposed on the fluid inlet (see Figure 8), taken from the experimental data. The boundary condition is translated in a constant velocity all over the inlet boundary. The inlet temperature is also specified, assumed to 27 °C, that is the average measured value during the tests. At the outlet boundary face the relative pressure is specified. On the symmetry planes (in green in Figure 8) a symmetry boundary condition is imposed, which means that the normal velocity and the normal gradients of all other variables are zero. Concerning the turbulent variables, for all the selected turbulence closures, constant values were imposed on the inlet while zero gradient condition is imposed on the outlet. A 3D, steady-state computational model was adopted.

The polyhedral mesh was used for the simulations by subdividing the domain in three zones of refinement, as shown in Figure 8b. The first zone includes the inlet and outlet pipes and the two manifolds and is characterized by the largest base size, equal to 0.6 mm, and 6 prism layers with a total thickness of the prism layer of 0.4 mm. The first refinement affects the two zones upstream and downstream of the MCs and is characterized by a base size of 0.5 mm. The third area is that of the MCs, characterized by the smallest cell size as it is shown in Figure 9, with a base size of 0.12 mm and 12 prism layers with a total thickness of 0.2 mm. Prism layers have been used for the wall treatment and the thickness of the first layer has been chosen to give $y^{+}\sim 1$ to cover the highest flow rate. A 3D representation of the finest mesh for the entire domain is reported in Figure 9c.

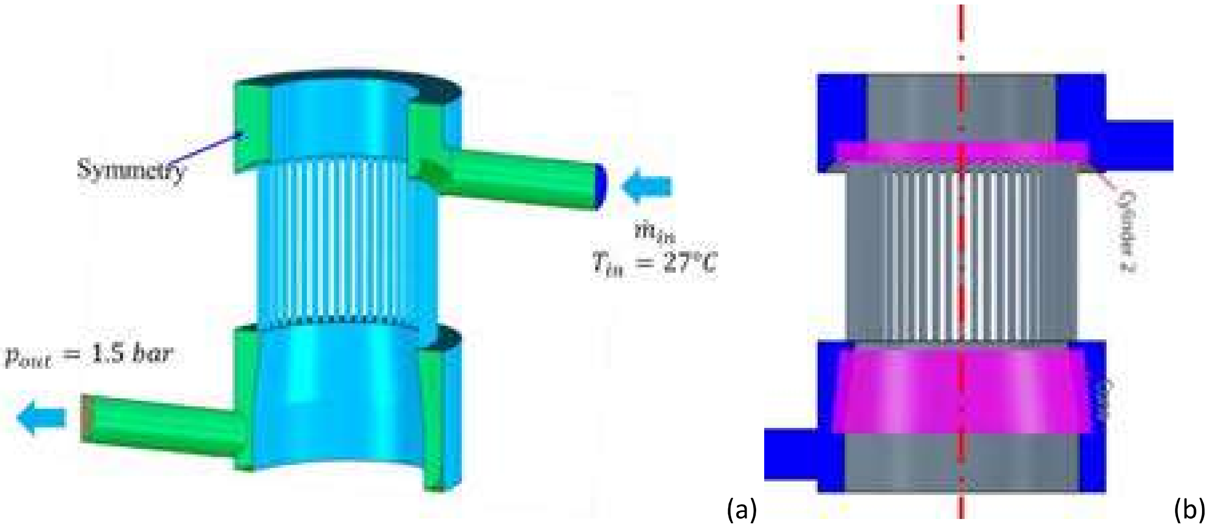

Figure 8: (a) Computational domain and boundary conditions for the fluid domain under investigation. Cyan surfaces are walls. (b) Subdivision of the three different zones of mesh refinement of the computational domain. The pink areas are characterized by the middle base size.

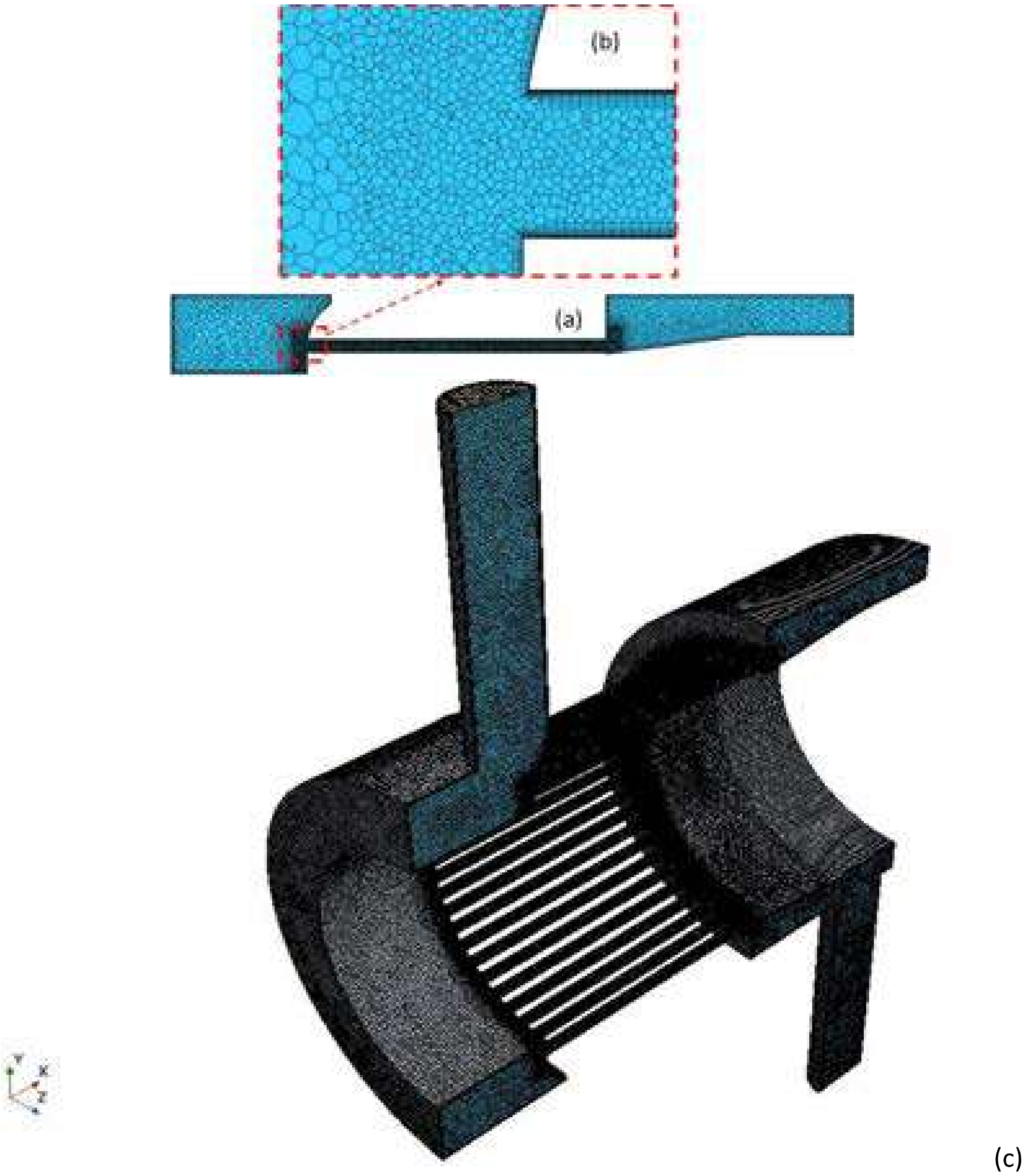

Figure 9: (a) Mesh representation on the axial section of the computational domain taken on the plain indicated with the red dashed line in Figure 8b. (b) Zoom of the mesh at the channel entrance. (c) 3D view of the mesh of the entire computational domain.

In Figure 10 the velocity maps at 50 l/min of flow rate in a longitudinal section of the mock-up are reported for the three turbulence models used in this study. With respect to the other, the $k - \omega\ SST$ presents on the longitudinal cross sections, taken at 90 degrees from the inlet (Sec. BB' in Figure 10) a higher velocity near the manifold wall, also corroborated with the velocity maps on the transverse section (Sec. AA' in Figure 10). At the same time, it shows a larger inlet effect in the MCs with the tendency to a swirl flow within the channels that is not so evident in the $k - \varepsilon$ models. At the channel outlet, the $k - \omega\ SST$ model presents a faster exit of the velocity with larger recirculation loops in the outlet manifold.

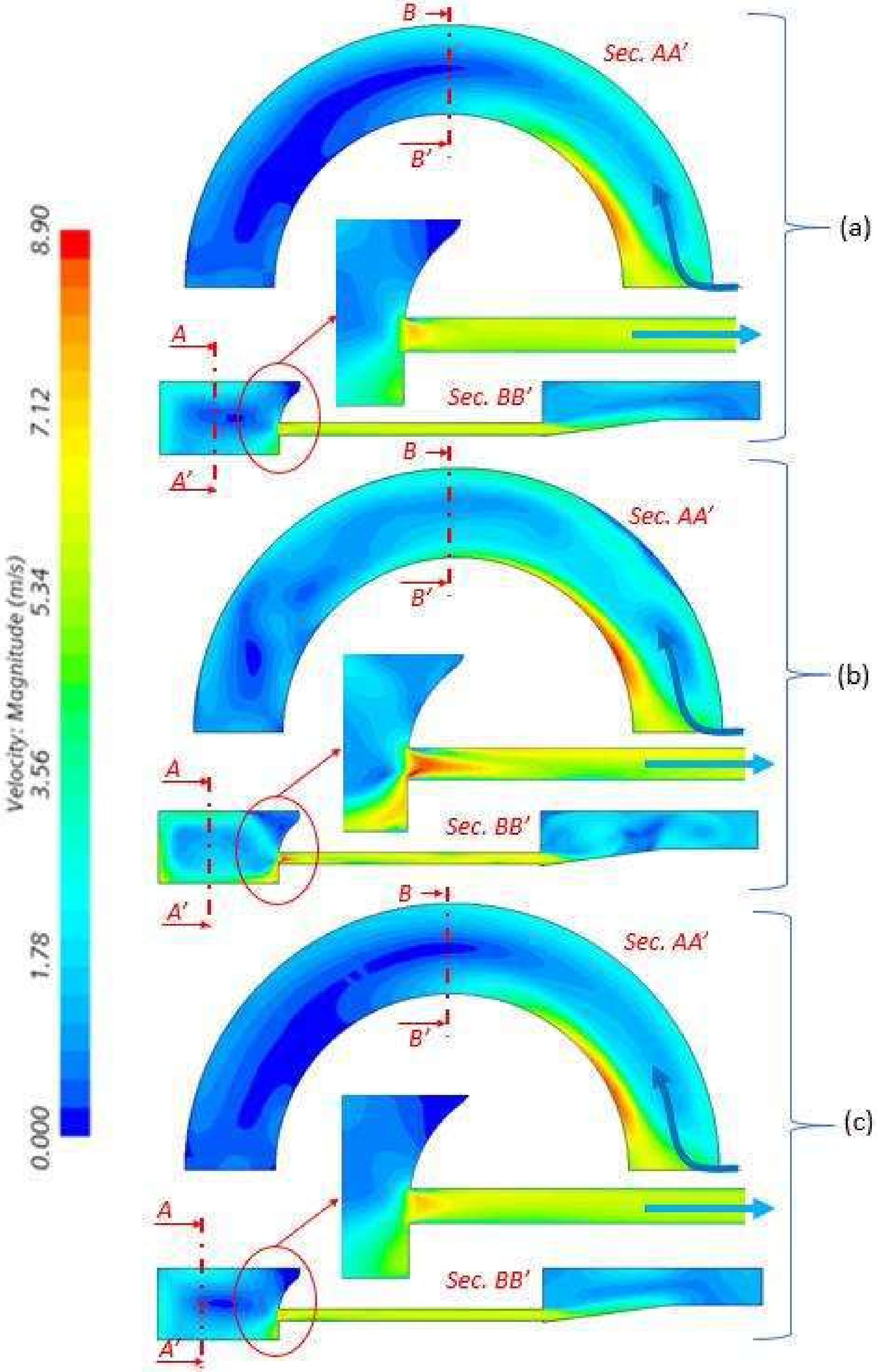

Figure 10: Velocity maps on one longitudinal and transverse section of the mock-up, for the three turbulence models: (a) Realizable $k-\varepsilon$, (b) $k-\omega\ SST$ and (c) Lag EB $k-\varepsilon$.

The mock-up pressure drop values are reported in Figure 7 comparing the simulations and experimental results with their associated uncertainties at each set point. While the results obtained from the *Realizable* $k-\varepsilon$ and $Lag\ EB\ k-\varepsilon$ models fall within the experimental uncertainty for almost the entire flow rate range, the values coming from the $k-\omega\ SST$ model show a consistent underestimation of the experimental vales. This mismatch grows in the $k-\omega\ SST$ simulation results as the flow rate increases. To evaluate the numerical uncertainty due to domain discretization in Figure 7, a grid convergence study was performed by progressively refining the area of the mini-channels only. Note that the mesh in the rest of the fluid was kept constant and previously defined in order to obtain mesh independent results. The characteristics of the mesh files used in the numerical uncertainty assessment are listed in Table 8. The observed order of convergence of the results was evaluated by mean of a Least Square method according to Eqs. 13-17, considering only the pressure drop characterizing the area interested by the mesh refinement. To evaluate the Grid Convergence Index (GCI) and the numerical uncertainties of each set point, the observed order of convergence for the simulation of the entire the mock-up was assumed the same of the MCs.

Table 8: Mesh parameters for GCI evaluation of the cavity mock-up pressure drops analysis.

	Entire Domain	Mini Channels		
Name	# Mcells	# Mcells	h (mm)	r_{i1}
1	9.75	6.05	0.152	1
2	6.31	3.72	0.179	1.12
3	3.56	2.05	0.219	1.37
4	2.77	1.63	0.236	1.47
5	1.97	1.04	0.274	1.71

The effect of the input parameter uncertainty on the global simulation uncertainty has been evaluated with reference to the inlet flow rate used as boundary conditions to the simulations, the uncertainty of which is taken as 0.5 l/min from the flow meter accuracy, and the channels diameter, affected by an uncertainty of 0.0005 m due to the manufacturing process, as shown in Figure 11. In order to quantify the effects of these two parameters, the sensitivity coefficients have been evaluated by adding and subtracting the uncertainty affecting each parameter in the different simulations.

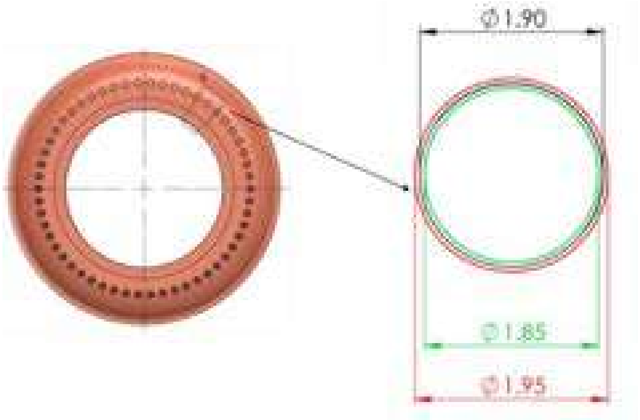

Figure 11: Channels Diameter uncertainty, used to drive the simulation input uncertainty.

4.3. Multivariate metric assessment

To check the effect of the correlation among different uncertainties on the final performance of the turbulence models, the multivariate metric assessment was performed as well, trying to identify how the uncertainties coming from the different sources interact.

Here the validation variable of the study is the pressure drop along the mock-up, which is the result of a data reduction equation of the actual measured pressures, see Eq. 27. None of the pressure measurements, however, is affecting as an input the simulations, where constant water properties are used. In order to analyze the contribution of the correlations of the uncertainty among the different set points (i.e., the pressured drops evaluated at different water flow rates) on the final result, two cases are considered:

Case a) in which the set points share no identical error source, and

Case b) in which all set points share identical error sources and the correlation among the different set point uncertainty is accounted for.

In *Case a*, the contribution of input simulation uncertainties and experimental uncertainties is evaluated neglecting any possible correlations as in Eq. 22, while for *Case b* Eq. 23 is used.

$$\boldsymbol{V}_{\boldsymbol{input+D}} = \begin{bmatrix} (X_{s,1} - X_{D,1})\boldsymbol{V}_{\boldsymbol{x,1}}(X_{s,1} - X_{D,1})^T & 0 & 0 \\ 0 & \ddots & 0 \\ 0 & 0 & (X_{s,n} - X_{D,n})\boldsymbol{V}_{\boldsymbol{x,n}}(X_{s,n} - X_{D,n})^T \end{bmatrix} \qquad \textit{Eq. 22}$$

$$\boldsymbol{V}_{\boldsymbol{input+D}} = (\boldsymbol{X}_s - \boldsymbol{X}_D)\boldsymbol{V}_X(\boldsymbol{X}_s - \boldsymbol{X}_{\boldsymbol{D}})^T \qquad \textit{Eq. 23}$$

In Eq. 22 (*Case a*), $X_{s,j}$ is a vector containing the m sensitivity coefficients for the simulations corresponding to each parameter affected by uncertainty for the $j-th$ set point. It is evaluated with Eq. 24 where the derivatives of the data reduction equation with respect to the different pressure measurements of the tests are null. $X_{D,j}$ is a vector containing the sensitivity coefficients for the data reduction equation for the $j-th$ set point and is evaluated with Eq. 25. In this case the sensitivity coefficients evaluated for the flow rate and channels diameter uncertainty are null. $\boldsymbol{V}_{\boldsymbol{x,j}}$ is the covariance matrix of the $j-th$ set point containing the m uncertainties of each parameter affected by uncertainty where all the off-diagonal terms are zero since no measured variables share an error source (Eq. 26).

Considering *Case b)* the covariance of the inputs at the multiple set points is identical to *Case a*. Therefore $\boldsymbol{V}_{\boldsymbol{x,1}} = \cdots = \boldsymbol{V}_{\boldsymbol{x,n}}$ and the covariance is evaluated using Eq. 26. The sensitivity matrixes are in turn defined by Eq. 27 and Eq. 28 where $X_{s,j}$ and $X_{D,j}$ are evaluated respectively with Eq. 24 and Eq. 25. The result of Eq. 23 is then a full matrix.

$$X_{s,j} = \begin{bmatrix} \frac{\partial S_j}{\partial x_1} & \dots & \frac{\partial S_j}{\partial x_m} \end{bmatrix} = \begin{bmatrix} \frac{\partial \Delta p}{\partial \dot{m}} & \frac{\partial \Delta p}{\partial d} & \frac{\partial \Delta p}{\partial p_{out_{tot}}} & \frac{\partial \Delta p}{\partial p_{in_{tot}}} & \frac{\partial \Delta p}{\partial p_{out_{loop}}} & \frac{\partial \Delta p}{\partial p_{in_{loop}}} \end{bmatrix} \qquad \textit{Eq. 24}$$

$$X_{D,j} = \begin{bmatrix} \frac{\partial D_j}{\partial x_1} & \dots & \frac{\partial D_j}{\partial x_m} \end{bmatrix} = \begin{bmatrix} \frac{\partial \Delta p}{\partial \dot{m}} & \frac{\partial \Delta p}{\partial d} & \frac{\partial \Delta p}{\partial p_{out_{tot}}} & \frac{\partial \Delta p}{\partial p_{in_{tot}}} & \frac{\partial \Delta p}{\partial p_{out_{loop}}} & \frac{\partial \Delta p}{\partial p_{in_{loop}}} \end{bmatrix} \qquad \textit{Eq. 25}$$

$$\boldsymbol{V}_{\boldsymbol{x,j}} = \begin{bmatrix} u_{x,1}^2 & \dots & 0 \\ \vdots & \ddots & 0 \\ 0 & \dots & u_{x,m}^2 \end{bmatrix} \qquad \textit{Eq. 26}$$

$$\boldsymbol{X_s} = \begin{bmatrix} X_{s,1} \\ \vdots \\ X_{s,n} \end{bmatrix} \qquad \textit{Eq. 27}$$

$$\boldsymbol{X_D} = \begin{bmatrix} X_{D,1} \\ \vdots \\ X_{D,n} \end{bmatrix} \qquad \textit{Eq. 28}$$

The results of the multivariate metric analysis for the three turbulence models are reported in Figure 12.

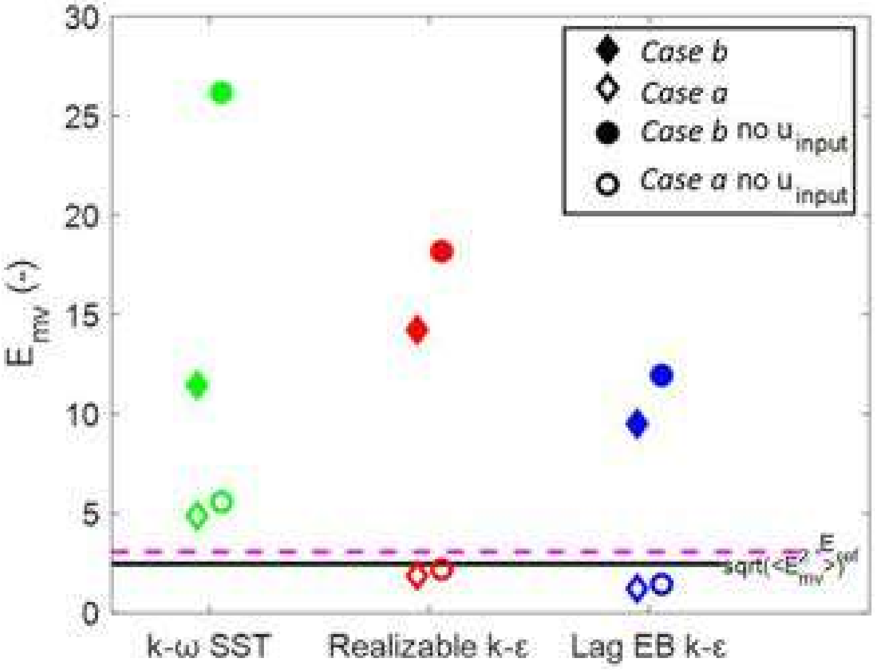

Figure 12: Results of the multivariate analysis on the MC mock-up for the four cases considered.

5. Results and discussion

The results of the hydraulic characteristic of a circular pipe in turbulent flow computed using the different turbulence models, when compared to the Colebrook correlation by mean of the multivariate metric presented above and collected in Figure 6, show a qualitative effect related on the accounting of common error source for the friction factor values. In the case the values of f are considered totally unaffected by shared error sources (Case *a)*), all three models show a similar performance, remaining lower than both the values of E_{ref} and $\sqrt{< E_{mv}^2 >}$, implying that the discrepancy between simulations and experiments can be justified by the correlation and numerical uncertainties. The result of the *Lag EB* $k-\varepsilon$ model is slightly lower than the other two while the *Realizable* $k-\varepsilon$ model shows the highest value. In Case *b)*, where the friction factor values from the Colebrook correlation are considered already somehow correlated by a common error source, the *Lag EB* $k-\varepsilon$ model is the only model to have an E_{mv} lower than the E_{ref}. This reveals that for the cases that the *Realizable* $k-\varepsilon$ and the $k-\omega$ *SST* models were used, the mismatch between the simulation results and the values from the Colebrook correlation cannot be justified only by all the uncertainties involved in the analysis, but the uncertainties are rather due to the models themselves. All in all, the *Realizable* $k-\varepsilon$ model has a poor performance in comparison with the other two models, while the *Lag EB* $k-\varepsilon$ model approaches the expected values of the Colebrook correlation more accurately.

Moving to the discussion results of the multivariate assessment of the three RANS models against the mock-up experimental outcome, in Figure 12, again a qualitative effect coming from the assumption on the common error source for the experimental data is clear. Observing the results for *Case a*, in which no identical error sources are considered, the E_{mv} evaluated for the two $k-\varepsilon$ models is lower than the reference value E_{ref} represented with the dashed line, while for the $k-\omega$ *SST* model it is above, ruling it out from the list of the recommended models for the investigated case study. This agrees with the results reported in Figure 7 where at high flow rate the error bar of the simulation results with $k-\omega$ SST does not lie in the error area of the experimental results. In *Case b*, i.e., accounting for the uncertainty correlation among the set points, for none of the selected models the discrepancy between simulated and experimental pressure drop can be justified only by the experimental data, input uncertainties as well as numerical uncertainties, and must be attributed to the adequacy / inadequacy of the model. However, *Lag EB* $k-\varepsilon$ turbulence model has the best performance to simulate pressure drop with a lower E_{mv} value with respect to the *Realizable* $k-\varepsilon$ models.

Note that if the uncertainty due to simulation input parameters was neglected, taking also the first derivatives of Eq. 24 as null, the E_{mv} would have increased for all models with a much larger effect on the $k-\omega$ SST model. However, the ranking of the three models remains the same even in that case.

6. Conclusions

A comparative platform to measure the fidelity and suitability of RANS models applied in modelling and simulation of mini-channel cavity cooling systems is successfully developed and evaluated. Two case studies were analysed, and namely: a circular smooth tube where simulations have been compared to a well-established correlation, and a gyrotron cavity mock-up equipped with mini-channels where simulations were compared to the experimental data. The same procedure for the comparison, involving a multivariate metric which can account for correlation among the different uncertainties affecting the data or the simulations was applied to the two cases.

In the analysis of the friction factor for the mini-channel, it was inferred that despite the presence of possible correlations in the uncertainty of the dataset used for the derivation of the Colebrook relation, the mismatches between the simulated values for f and the theoretical ones can be justified only by the experimental data and numerical uncertainties if the *Lag EB* $k-\varepsilon$ turbulence model is adopted. Furthermore, in the analysis of the mock-up hydraulic characteristic, the *Lag EB* $k-\varepsilon$ turbulence model had a better performance among the three analysed to predict the friction factor in the MCs device. However, if correlation among the different set point uncertainty is accounted, since the data points share identical error sources, the discrepancy between all the simulation sets and the experimental data cannot be simply justified by the experimental and numerical uncertainties ($E_{mv} > E_{ref}$), even if one accounts for the input uncertainty to the simulations. In this picture, the *Lag EB* $k-\varepsilon$ returns in all cases better results than the other two models. If the correlation between the uncertainty of the experimental points is neglected, the two $k-\varepsilon$ models give results within the numerical/experimental uncertainty. Both models could be then considered reliable if the uncertainty assessment is performed solely based on a single-point metric, revealing how a multivariate metric allows capturing overall features that are not visible otherwise, when the correlation among uncertainties is accounted for.

The better outcome generated by using the *Lag EB* $k-\varepsilon$ model can be explained by the nature of the turbulence model since a complex flow path with several curves and rotations along the flow assists a model reproducing to some extent the asymptotic near-wall behaviour of the different (anisotropic) Reynolds stresses. As the main outcome of the work presented here, future studies involving gyrotron cavities equipped with mini-channels using the *Lag EB* $k-\varepsilon$ turbulence model will be performed accordingly.

Further validation addressing the heat transfer simulations is needed due to the different formula used in the *Lag EB* $k-\varepsilon$ model to evaluate the eddy turbulence viscosity. That is used to evaluate the turbulence term of the stress tensor which appears in the energy equation.

Acknowledgements

The authors are grateful to Mr. A. Allio (Politecnico di Torino) and to the ASME V&V 20 committee for helpful discussion and support. We also acknowledge the use of the computational resources provided by hpc@polito, which is a project of Academic Computing within the Department of Control and Computer Engineering at the Politecnico di Torino (http://hpc.polito.it).

References

[1] M. K. A. Thumm, G. G. Denisov, K. Sakamoto, and M. Q. Tran, “High-power gyrotrons for electron cyclotron heating and current drive,” *Nuclear Fusion*, vol. 59, no. 7. 2019, doi: 10.1088/1741-4326/ab2005.

[2] A. Kasugai, K. Sakamoto, K. Takahashi, K. Kajiwara, and N. Kobayashi, “Steady-state operation of 170 GHz–1 MW gyrotron for ITER,” *Nucl. Fusion*, vol. 48, no. 5, p. 054009, Apr. 2008, doi: 10.1088/0029-5515/48/5/054009.

[3] K. Sakamoto *et al.*, “Development of high power gyrotron for ITER application,” *IRMMW-THz 2010 - 35th Int. Conf. Infrared, Millimeter, Terahertz Waves, Conf. Guid.*, 2010, doi: 10.1109/ICIMW.2010.5613016.

[4] A. G. Litvak *et al.*, “Development of 170 GHz/ 1MW/ 50%/ CW gyrotron for ITER,” pp. 111–112, Oct. 2006, doi: 10.1109/ICIMW.2004.1421978.

[5] J. Jelonnek *et al.*, “From W7-X Towards ITER and Beyond: 2019 Status on EU Fusion Gyrotron Developments,” 2019, doi: 10.1109/IVEC.2019.8744989.

[6] Z. C. Ioannidis *et al.*, “First CW experiments with the EU ITER 1 MW, 170 GHz industrial prototype gyrotron,” *IVEC 2017 - 18th Int. Vac. Electron. Conf.*, vol. 2018-Janua, pp. 1–2, Feb. 2018, doi: 10.1109/IVEC.2017.8289742.

[7] J. Jelonnek *et al.*, “Design considerations for future DEMO gyrotrons: A review on related gyrotron activities within EUROfusion,” *Fusion Eng. Des.*, 2017, doi: 10.1016/j.fusengdes.2017.01.047.

[8] K. A. Avramidis *et al.*, “Towards a 1.5 MW, 140 GHz gyrotron for the upgraded ECRH system at W7-X,” *Fusion Eng. Des.*, vol. 164, p. 112173, Mar. 2021, doi: 10.1016/J.FUSENGDES.2020.112173.

[9] R. Marchesin *et al.*, “Manufacturing and Test of the 1 MW Long-Pulse 84/126 GHz Dual-Frequency Gyrotron for TCV,” *2019 Int. Vac. Electron. Conf. IVEC 2019*, Apr. 2019, doi: 10.1109/IVEC.2019.8745147.

[10] “gyrotron.” https://archive.org/details/gyrotron.

[11] “Classic Kit: Raschig’s rings | Opinion | Chemistry World.” https://www.chemistryworld.com/opinion/classic-kit-raschigs-rings/3004935.article (accessed Sep. 07, 2021).

[12] A. Bertinetti *et al.*, “Multi-physics analysis of a 1 MW gyrotron cavity cooled by mini-channels,” *Fusion Eng. Des.*, vol. 123, pp. 313–316, Nov. 2017, doi: 10.1016/J.FUSENGDES.2017.05.016.

[13] A. Allio, R. Difonzo, A. Leggieri, F. Legrand, R. Marchesin, and L. Savoldi, “Test and Modeling of the Hydraulic Performance of High-Efficiency Cooling Configurations for Gyrotron Resonance Cavities,” *Energies 2020, Vol. 13, Page 1163*, vol. 13, no. 5, p. 1163, Mar. 2020, doi: 10.3390/EN13051163.

[14] A. Bertinetti *et al.*, “Multi-physics analysis of a 1 MW gyrotron cavity cooled by mini-channels,” *Fusion Eng. Des.*, 2017, doi: 10.1016/j.fusengdes.2017.05.016.

[15] P. C. Kalaria *et al.*, “Design Studies of Mini-Channel Cavity Cooling for a 170 GHz, 2 MW Coaxial-Cavity Gyrotron,” *2019 Int. Vac. Electron. Conf. IVEC 2019*, Apr. 2019, doi: 10.1109/IVEC.2019.8745135.

[16] W. Rao *et al.*, “Thermal Analysis of Micro-Channel Cooling for a Megawatt Gyrotron Travelling Wave Tube,” *2019 Int. Vac. Electron. Conf. IVEC 2019*, Apr. 2019, doi: 10.1109/IVEC.2019.8744690.

[17] The American Society of Mechanical Engineers (ASME), *Supplement to ASME V&V 20-2009 – Multivariate Metric for Validation*. 2021.

[18] Siemens Digital Industries Software, Simcenter STAR-CCM+ User Guide v2021.1, Siemens 2021.

[19] T. H. Shih, W. W. Liou, A. Shabbir, Z. Yang, and J. Zhu, “A new k-ϵ eddy viscosity model for high reynolds number turbulent flows,” *Comput. Fluids*, vol. 24, no. 3, pp. 227–238, Mar. 1995, doi: 10.1016/0045-7930(94)00032-T.

[20] H. K. Versteeg and W. Malalasekera, *An Introduction to Computational Fluid Dynamics Second Edition*. 2007.

[21] F. R. Menter, “Two-equation eddy-viscosity turbulence models for engineering applications,” *AIAA J.*, vol. 32, no. 8, pp. 1598–1605, 1994, doi: https://doi.org/10.2514/3.12149 PDF PDF Plus.

[22] S. Lardeau and F. Billard, “Development of an elliptic-blending lag model for industrial applications,” *54th AIAA Aerosp. Sci. Meet.*, vol. 0, 2016, doi: 10.2514/6.2016-1600.

[23] The American Society of Mechanical Engineers (ASME), *Standard for Verification and Validation in Computational Fluid Dynamics and Heat Transfer*. 2009, pp. 1–26.

[24] P. Gerhart, A. Gerhart, and J. Hochstein, *Munson’s Fluid Mechanics*. Wiley, 2017.

Declaration of interests

☒The authors declare that they have no known competing financial interests or personal relationships that could have appeared to influence the work reported in this paper.

☐The authors declare the following financial interests/personal relationships which may be considered as potential competing interests:

Author statement for the manuscript "Assessment of different RANS turbulence models in mini-channels for the cooling of MW-class gyrotron resonators"

Rosa Difonzo: Conceptualization, Methodology, Software, Formal analysis, Investigation, Validation, Data curation, Visualization, Writing - Original Draft

Eleonora Gajetti: Methodology, Software, Investigation, Validation, Visualization, Writing - Original Draft

Laura Savoldi: Conceptualization, Methodology, Investigation, Resources, Supervision, Writing - Review & Editing

Nima Fathi: Methodology, Writing - Review & Editing.